MECH3790: Wind Tunnel Lab Report

Harry Fotheringham

November 2023

SID: 201419355
Program of Study: MEng Aeronautical and Aerospace Engineering
Year of Study: 3
Module number: MECH3790
Session Attended: 08/11/23

UNIVERSITY OF LEEDS

Contents

Aerofoil	Cruise C_L	Cruise Altitude (km)	Cruise Speed (m/s)	Wind chord (m)
NACA2412	0.44	5.88	58.07	1.43

Table 1: Aircraft configuration parameters at cruise

0.1 Aerofoil Specifications

1 Question 1 - Wind Tunnel Laboratory

1.1 Part i - Calculate the flow Reynolds Number with respect to the chord length, *c* of the aerofoil

To calculate the flow Reynolds number R_e Equation 1 is used.

$$R_e = \frac{\rho V L}{u} \tag{1}$$

This means that the air density, air velocity and dynamic viscosity of air must all be calculated. From the question, L is equal to the chord length, c which is given to be $12cm$ [14]. The temperature of the air was measured to be $15°C$, using this value dynamic viscosity of air can be assumed to be $17.89 \times 10^{-6} Pa.s$ [3].

To calculate the value for air density ρ_{air} we used a barometer. The barometer measured the height of the mercury to be $739.5mm$. First, by using this value and a value of $13545.848kg/m^3$ for the density of mercury into Equation 2 the air pressure in the room was found to be $98268Pa$.

$$P = \rho_{mercury} g h \tag{2}$$

Then by using this pressure with the specific gas constant, R ($287.26J/kg/K$ [12]) and the temperature ($288K$) from a thermometer in the room in Equation 3, the air density was found to be $1.1878kg/m^3$. These values seem sensible as the typical values for air pressure and density are $101.325kPa$ [4] and $1.2256kg/m^3$ [5] respectively, which are close to the final values.

$$\rho_{air} = \frac{P}{RT} \tag{3}$$

Finally, to find the airspeed we use the value that is calculated from Section 1.2. Using these values in Equation 1 the Reynolds number was calculated to be 1.4584×10^5, as shown in 4.

$$R_e = \frac{1.1878 \times 18.31 \times 0.12}{17.98 \times 10^{-6}} = 1.4584 \times 10^5 \tag{4}$$

1.2 Part ii - Calculate the free stream velocity U_∞ at the wind tunnel test section

In the Laboratory we used a Pitot Tube to calculate U_∞. From the Pitot Tube, a pressure difference of $1.99mBar$ was measured, which is equivalent to $199Pa$. To find U_∞ from this we need to use Bernoulli's Equation Equation 5. To use this equation, some assumptions about the flow in the wind tunnel must be made. The flow is considered steady, streamlined, incompressible and inviscid.

$$P_1 + \frac{1}{2}\rho V_1^2 = P_2 + \frac{1}{2}\rho V_2^2 \tag{5}$$

From this equation, we can make some further simplifications as we know $V_1 = 0$ and $V_2 = V_\infty$. This is because the Pitot tube measures the stagnation pressure (total pressure), which occurs when the fluid comes to rest. Therefore, we know at this point, the velocity of the fluid (V_1) is zero. This means that the static pressure difference is equal to the dynamic pressure induced by the free stream. This results in Equation 6.

$$\Delta P = \frac{1}{2}\rho V_\infty^2 \tag{6}$$

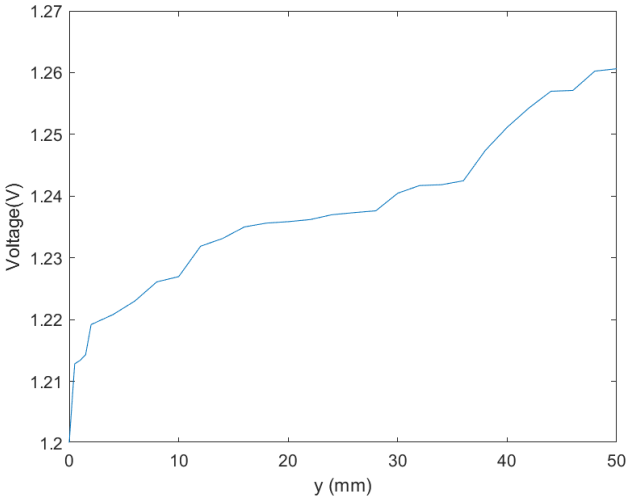

Figure 1: Shows a plot of the voltage (V) through the hotwire probe measure at a specific height (mm) of the probe for the NACA 2412 Aerofoil.

Re-arranging this equation it becomes:

$$V_\infty = \sqrt{\frac{2(\Delta P)}{\rho}} \tag{7}$$

Once we have all of these known values on the right-hand side of the equations we can solve for free stream velocity. We know that the pressure difference is $199Pa$ and the air density which was calculated in Section 1.1 is $1.1878kg/m^3$. This means that the free stream velocity can be calculated to be $18.31m/s$ which aligns with the initial specification given suggesting that the velocity can be anything up to $21m/s$ [14].

$$V_\infty = \sqrt{\frac{2(199)}{1.1878}} = 18.31m/s \tag{8}$$

1.3 Part iii - Plot of V vs y

1.4 Part iv - Potential sources of error in the wind tunnel test

Several different errors could occur when performing this kind of wind tunnel test. Some of them are listed in Table 2.

1.5 Part v - How could drag be predicted if measuring air speed before and after the aerofoil? Why is this more accurate than the near-field method?

The way to calculate the drag is by using the integral form of the momentum equation also known as the far-field method. This method uses the change in momentum from the free stream compared to the wake to predict the drag as the drag results from a loss in the momentum. Therefore, if we measure the velocities upstream and downstream and work out the difference we can find the drag force. Equation 9 shows the governing equation for this process. The ' symbol here is used to denote that it is drag per unit span. In other words, we are assuming that we have a 2D aerofoil. If we examine Equation 9 more closely we can see that $u_1 - u_2$ is the velocity decrement for a given y location between h and b which are both located on Figure 2. It is clear that in the wake there is a loss in the flow velocity. The quantity ρu_2 is the mass flux and when multiplied by the velocity decrement it gives the change in momentum. From Newton's second law, we know the force is equal to a change in momentum. So from this, we can see that the change in wake

Potential Error	Effect
Wing impurities, such as scratches or rivets	These will affect the airflow and provide more drag to the wing. As it is such a small model it is likely these effects will be more prevalent than on a large aircraft
Tape on the bottom of the wind tunnel	The tape kept coming loose which will have affected the airflow across the aerofoil.
Height inaccuracy	Turning the wheel to heighten the rod, it was easy to lose track of rotation count. There was also no way of accurately knowing the correct position as the increment was just marked with a thick pen marker.
Ideal Flow assumptions in calculations	To perform calculations to determine free stream velocity we used Bernoulli's Equation suggesting that the flow was steady, inviscid, incompressible and irrotational. However, this is unlikely to be the case.
Alignment of the pitot tube	The pitot tube may not have been perfectly parallel with the flow, meaning that the pressure that was determined may be inaccurate.
Calibration errors	If the probe is not properly calibrated, it can introduce systematic errors into the measurements
System errors	When the data was recorded there was a lot of electrical noise which meant that we needed to take an average over all of the data points. However, this average may be incorrect.

Table 2: Shows the different errors that could have occurred while performing this experiment and the effect this could have on the results

momentum is equal to the drag on the body. Here we have assumed that the flow is incompressible so ρ is constant throughout the wind tunnel [6].

$$D' = \rho \int_h^b u_2(u_1 - u_2)dy \tag{9}$$

Using this method is more accurate than the near-field method because of potential rounding errors because Drag is typically much smaller than lift for an aerofoil. If we consider both components of drag, tangential and normal, because of the slight slope along the surface of the aerofoil the tangential component becomes much smaller than the normal component, which can also lead to rounding errors. The far-field method also considers the flow further away from the aerofoil taking into account the effect of the whole aerofoil shape whereas the near-field method considers flows close to the surface of the aerofoil meaning that viscous forces play a larger effect. The far-field method is also much less sensitive to boundary layer effects as the flow momentum is being measured before and after it has interacted with the aerofoil. However, this method

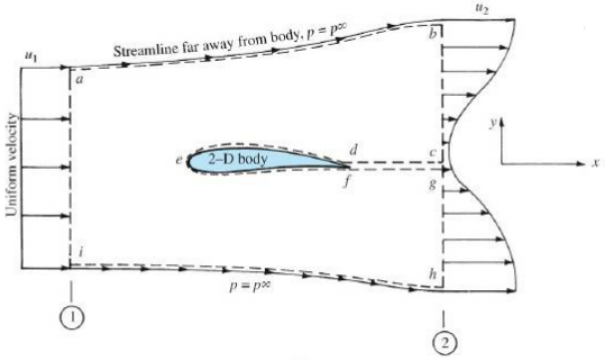

Figure 2: Control volume for obtaining drag on a two-dimensional body [6][page 132g]

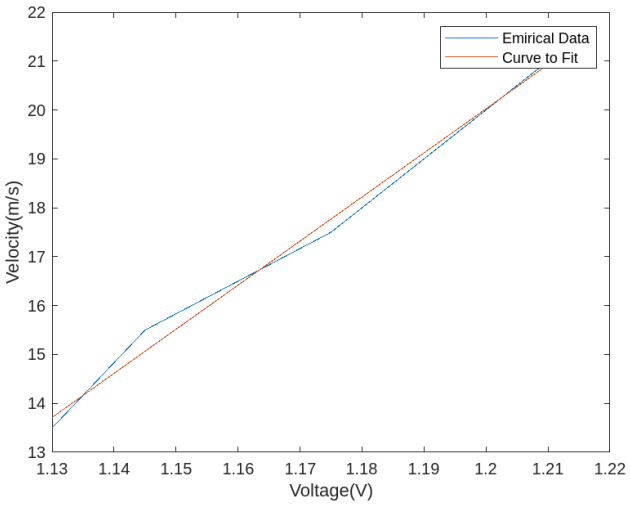

Figure 3: Shows the Empirical data for velocity measured against voltage and then a line of best fit is plotted through to represent the linear relationship so that the voltage measured can be converted into a velocity value.

neglects the surface shear stresses as any shear stresses or pressure distributions along the upper or lower surface cancel each other out.

1.6 Part vi - How to calculate drag from the from the data collected? What assumptions do we make so that the method mentioned in (v) becomes applicable?

To calculate the drag from the data that we collected we can use the far-field method that has been briefly mentioned in the previous section. This uses Equation 9. For this particular experiment, the density would be the density of the air which was measured as $1.1878kg/m^3$. The initial air velocity, u_1 , is equal to the free stream velocity, U_∞, which is calculated as $18.31m/s$. For h and b the lower height and the maximum height of the hot wire probe are used respectively. To get the velocity after the aerofoil, u_2, we can use the calibration curve shown in Figure 3. A line of best fit can be plotted through the curve shown in red and this line can be used to read off the velocity for each of the different heights of the probe. With all of the data, we can integrate over the full range of the probe and find the drag that is produced by the change in momentum of the air. Due to the amount of data, numerical methods should be used to calculate the value of the drag. For at least every 2mm change in the height of the probe, there is a new u_2 value. This means all of these values will need to be summed over the full range of the probe to find the overall change in momentum caused by the aerfoil.

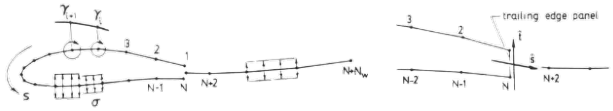

Figure 4: Aerofoil and wake panelling with vorticity and source distributions as well as the detail of the trailing edge [8].

2 Question 2 - Research to explain the theoretical basis of the XFoil method and the advantages and disadvantages relative to higher fidelity CFD methods that typically solve the RANS equations

The XFoil software was created in 1986 by Mark Drela, a professor at MIT. It combines the potential flow panel method with a fully coupled inviscid/viscous interaction method [9, 11]. It was developed to formulate a rapid solution to predict the aerofoil performance at a set Reynolds number. There are 3 different formulations that can be completed by this software:

1. Inviscid Formulation
2. Inverse Formulation
3. Viscous Formulation

2.1 Inviscid Formulation

The most straightforward of the 3 is the inviscid formulation. This assumes that the flow is inviscid and uses a linear-vorticity stream panel method, with a trailing edge thickness modelled with a source panel. This can be seen from Figure 4. By superposing the freestream flow over the aerofoil, a vortex sheet with strength γ on the aerofoil surface, and another source sheet of strength σ on the aerofoil surface and wake [8]. The stream function related to this configuration is given by Equation 10.

$$\Psi(x,y) = u_\infty y - v_\infty x + \frac{1}{2\pi}\int \gamma(s)\ln r(s;x,y)ds + \frac{1}{2\pi}\int \sigma(s)\theta(s;x,y)ds \tag{10}$$

As shown in Figure 4 the contour of the aerofoil and and the trajectory of the wake are split into flat panels with N number of nodes on the aerofoil and N_ω number of nodes on the wake. Each panel has a constant source strength and each panel on the aerofoil has a linear vorticity distribution. Across the trailing edge of the tail, there must also be a uniform source strength and a uniform vortex strength for it to have a finite thickness. This equation is then linearised by requiring that the stream function is equal to some constant value at each node. This linear system is then combined with the Kutta condition, which states that the circulation around and aerofoil is fixed such that the flow leaves the trailing edge smoothly [6]. Where the geometry is known this combination can be solved by Gaussian elimination which gives the surface vorticity values, which is shown in Equation 11.

$$\gamma_i = \gamma_{0_i}\cos\alpha + \gamma_{90_i}\sin\alpha + \sum_{j=1}^{N+N_w-1} b'_{ij}\sigma_i \tag{11}$$

This is for inviscid flow where the source strengths are known so a solution can be immediately obtained. Whereas for viscous flows the source strength is unknown and must be augmented with boundary layer equations to find a solution. [8].

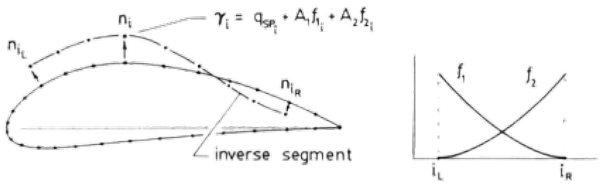

Figure 5: The problem with the vorticity matrix due to the inverse segment.

2.2 Inverse Formulation

The next formulation is the Inverse formulation. This formulation occurs when some of the geometry of the aerofoil is known and the surface vorticity or speed is known for the remaining area of the aerofoil. This means that at each node there is one unknown either the vorticity or the geometric displacement. To find the surface vorticity of a node in the inverse section, two free parameters A_1 and A_2 are added to the specified vorticity distribution. It is necessary to add the two degrees of freedom to the specified vorticity to allow geometric continuity along the aerofoil. This is required where the two nodes exist that join the inverse section to the fixed part of the aerofoil. In this case, the same governing stream function as before can be used (Equation 10). Because this is the case, a Newton-Raphson procedure is required to solve the overall system. By eliminating the source distribution so that only the inviscid inverse problem is treated and by applying the geometric continuity with the Kutta condition the solution around one node can be linearised. Leaving us with what is referred to as a Newton system. The stream functions of each one of the panels can be differentiated using the chain rule and the inverse solution solved by repeatedly solving the Newton system for the variable changes and updating the current variables. Usually, between two and four solutions are required to converge, but this is heavily dependent on how much the aerofoil geometry is to change. With the same number of panels roughly the same computational effort is required for an inviscid calculation [8].

2.3 Viscous Formulation

The third formulation is the most complex and allows the solving of viscous flows. To do this it takes into account viscous flows over the aerofoil and uses a very similar code to ISES [7], with some slight adjustments to improve the prediction of base drag from a blunt trailing edge. This method uses standard compressible integral momentum and kinetic energy shape parameter equations (Equations 12,13), where the streamwise coordinate is ξ.

$$\frac{d\theta}{d\xi} + (2 + H - M_e^2)\frac{\theta}{u_e}\frac{du_e}{d\xi} = \frac{C_f}{2} \tag{12}$$

$$\theta\frac{dH^*}{d\xi} + (2H^{**} + H^*(1 - H))\frac{\theta}{u_e}\frac{du_e}{d\xi} = 2C_D - H^*\frac{C_f}{2} \tag{13}$$

To account for deviations in the outer layer dissipation coefficient, C_D a maximum shear stress coefficient, C_T is used.

$$\frac{\delta}{C_T}\frac{dC_T}{D\xi} = 5.6\left(C_{T_{EQ}}^{1/2} - C_T^{1/2}\right) + 2\delta\left\{\frac{4}{3\delta^*}\left[\frac{C_f}{2} - (\frac{H_k - 1}{6.7H_k})^2\right] - \frac{1}{u_e}\frac{du_e}{d\xi}\right\} \tag{14}$$

For laminar flow regions, a different formulation is used than the one shown in Equation 14. It is replaced by a rate equation that models the change of the amplitude $\tilde{n}$ of the most amplified Tollmen-Schlichting curve.

$$\frac{d\tilde{n}}{d\xi} = \frac{d\tilde{n}}{dRe_\theta}(H_k)\frac{dRe_\theta}{d\xi}(H_k, \theta) \tag{15}$$

Equation 15 contains two different relations. The first one is an empirical relation $d\tilde{n}/dRe_\theta(H_k)$, which is a correlation of spatial growth rates determined from the Orr-Sommerfeld equation. This is combined with another relation $dRe_\theta/d\xi(H_k, \theta)$, which is found in the properties of the Falkner-Skan profile family. The transition point of the equation is determined from where $\tilde{n} = \tilde{n}_{crit}$ that the user will specify. In a physical

sense, this is used to represent the background disturbance level, which at a low Reynolds number can have quite a considerable effect on the aerofoil performance [8].

The fundamental variables used by the boundary layer equations are $\theta, \delta*$ and C_T except in the case where flow is laminar. In this case, C_T can be replaced with $\tilde{n}$. Moreover, u_e is an external unknown which will be linked to the global viscous solution through the inviscid outer flow. From these variables, auxiliary variables can be defined in terms of these variables. These are detailed in [8].

Moving on to the model of the wake now, this is treated as a single viscous layer so only one θ and one δ^* variable is present in each station of the wake. The initial conditions at the trailing edge are shown in Equation 16.

$$\theta_{wake} = \theta_{upper} + \theta_{lower} \qquad \delta^*_{wake} + \delta^*_{upper} + \delta^*_{lower} + h_{TE} \tag{16}$$

Even with a blunt edge, this creates a continuous displacement body with a thickness of h_{TE}. The initial wake shear coefficient is considered the θ-weighted average of the upper and lower surface values. This is shown in Equation 17.

$$C_{T_{wake}} = \frac{C_{T_{upper}}\theta_{upper} + C_{T_{lower}}\theta_{lower}}{\theta_{upper} + \theta_{lower}} \tag{17}$$

Equations 12,13,14,15 can all be discredited using the trapezium method, with each one of the boundary layer variables defined to be located at the different specific panel nodes. This leaves each aerofoil with three coupled non-linear equations associated with them that can be solved [8].

The flow inside the aerofoil is considered stationary meaning on the outer surface of the aerofoil u_e is equal to the vorticity on the suction side and the negative vorticity on the pressure side. This is for the aerofoil but when considering the wake there is no such relationship that exists therefore u_e must be related to the free stream and a sum of all the vorticity and sources along the aerofoil. The effect of the viscous layer on the potential flow is modelled by the wall transpiration concept if the local source strength is equivalent to the local gradient of the mass defect, m. This is shown in Equation 18

$$\sigma_i = \frac{dm}{d\xi} = \pm\frac{m_{i+1} - m_i}{s_{i+1} - s_i} \tag{18}$$

Combining the general expression for the surface vorticity (Equation 11) with the expressions for u_e at a specific node and then eliminating the source strength in terms of the mass defect produces Equation 19.

$$u_{e_i} = u_{INV_i} + \sum_{j=1}^{N+N_w-1} d_{ij} m_i \tag{19}$$

This is a very general equation that is used to find the solution about the aerofoil for any distribution of mass defect on either the wake or the aerofoil or both. The equation can be solved using a full Newton method and the Newton system takes the form of Equation 20 [8].

$$[J_{ij}] \begin{Bmatrix} \delta\theta_i \\ \delta m_i \\ \delta\tilde{n}_j, \delta C_{Tj} \end{Bmatrix} = \{-R_i\} \tag{20}$$

2.4 Compressible Flow

Finally to account for compressible flow regions a Karman-Tsein compressibility correction is integrated into the model [9]. This determines an approximate value for the compressible speed q and the pressure coefficient C_p on the aerofoil using incompressible flow values, q_{inc}, $C_{p_{inc}}$. The two equations used for this calculation are shown in Equation 21.

$$C_p = \frac{C_{p_{inc}}}{\beta + \lambda(1+\beta)C_{p_{inc}}/2} \qquad q = \frac{q_{inc}(1-\lambda)}{1 - \lambda(q/q_\infty)^2_{inc}} \tag{21}$$

All the calculations performed for compressible flow assume that the aerofoil surface vorticity represents the incompressible speed, q_{inc}. That means that overall the Equation 21 is only used to find C_p for lift and momentum calculations. In conjunction with the boundary layer formulation, viscous effects u_e seen

by the boundary layer are calculated. The boundary layer itself is already applicable for compressible flows so requires no correction [8]. Formulations incorporate a Karman-Tsien compressibility correction into the analysis meaning analysis on compressible flows can be completed and is highly accurate when performing an analysis in regions up to sonic. However, once the sonic threshold has been exceeded and the speed is above Mach 1 the Karman-Tsien correction breaks down, so once the transonic region has been reached the accuracy of the correction rapidly decreases. Consequently, once shocked flows are involved there is no way to predict the effect with any certainty using XFoil.

2.5 Advantages and Disadvantages

When it comes to the XFoil software it is very beneficial to perform accurate rapid computation. As mentioned in the documentation [9] the software was generated with the main goal in mind of combining the speed and accuracy of high-order panel methods with new fully-coupled viscous/inviscid interaction. Therefore, speed and accuracy are at its core so it seems trivial that it performs rapid and accurate analysis of aerofoils. The vast database of aerofoils built into the software with the added ability to add your own vastly improves the user's experience rather than having to enter all of the details for the aerofoil of interest manually. It also produces highly accurate results that have been found very close to experimental data [15]. The software is also relatively easy to use, due to the simplistic nature with some fluid flow knowledge it is quick to get comfortable with XFoil. But this package is limited to lower Reynolds numbers and can only represent aerofoils in 2D space. It also has limitations going above sonic flow velocities and cannot predict the effect this will have on the aerofoil.

Other packages that can analyse flow over an aerofoil are computational fluid dynamics software packages. Some examples include Autodesk CFD, SimScale, Ansys and openFOAM. These types of software packages solve higher-order equations, typically the RANS equation which allows for much more functionality. The RANS equation is the Reynolds-Averaged Navier-Stokes equation. These software have a much higher versatility than XFoil as they can handle a wide range of 3D flow patterns. They can analyse the effect of the flow in 3 dimensional space as well and take into account the roughness of the aerofoil surface. It is also possible to model a boundary layer with these software which is important when trying to make simulations as realistic as possible. The information that is output from a CFD analysis is much more detailed than for XFoil and provides information like pressure distribution and the behaviour of the fluid at different points in 3D space. However, with all these features learning to us a CFD software like this was can be very challenging for a beginner unlike XFoil. The more complex the model is made the more computational power that will be required from the computer. Finally, due to the nature of the RANS equation relying on turbulence models, inaccuracy could be incorporated into the analysis in this way especially for extremely complex flows.

3 Question 3 - Assume that boundary-layer transition occurs at 5% chord on both upper and lower surfaces of the wing, at the given cruise condition of the Cessna 172 (see Table 1) provide a description of the aerofoil's performance (i.e. in terms of lift and drag coefficient) over a range of angle of attack α. Discuss the underlying flow physics in terms of pressure distribution, stagnation point position and boundary layer characteristics in each case. You may assume the wing of the aircraft is two-dimensional, i.e. the wing has an infinite wing span

3.1 Method

To find the effect of the changing angle of attack, α on the NACA Aerofoil, the XFoil software explained in Section 2 can be used. From the question, the key information is:

- boundary layer occurs at 5% of the chord on the upper and lower surfaces of the wing
- At the cruise condition
- Provide a list of lift and drag coefficients over a range of angles of attack
- Produce a predicted lift and drag coefficient polar
- Plot a chord-wise pressure coefficient for each angle of attack
- For each case discuss the flow physics in terms of stagnation point, boundary layer
- The wing of the aircraft is assumed to have an infinity span

Next, the Reynolds number was calculated using the assumption of an International Standard Atmosphere and the data from Table 1. From Table 1 it is clear that the altitude is $5.88km$. By using the ISA assumption the atmosphere is presumed 'still', i.e. the air is stationary and only the aircraft is moving, so the velocity is $58.07m/s$. It is also known that Density, ρ_0, Temperature, T_0 and Dynamic Viscosity, μ_0 at sea level are $1.2256kg/m^3$, $288.15K$ and $1.458 \times 10^{-5} Pa.s$ respectively.

To calculate the Reynolds number 1 was used. This dynamic viscosity and air density need to be calculated for the aircraft's altitude at cruise. The first step is to use Equation 22 to find the temperature of the air at the cruising altitude. The Lapse Rate, L and Specific Gas Constant, R are assumed to be $0.0065K/m$ and $287.26J/kg/K$ from the ISA.

$$T_{altitude} = T_0 - Altitude \times L \tag{22}$$

Following on from this the temperature at altitude can be used to calculate the density, which is shown in Equation 23.

$$\rho_{altitude} = \rho_0 \times \frac{T_{altitude}}{T_0}^{\frac{g}{LR}-1} \tag{23}$$

Finally, the dynamic viscosity can be calculated using Equation 24

$$\mu_{altitude} = \mu_0 \times \frac{T_{altitude}^{1.5}}{T_{altitude} + 110.4} \tag{24}$$

Using these equations the temperature at altitude is calculated to be $249.93K$, the density can be calculated to be $6690kg/m^3$ and the dynamic viscosity is viscosity altitude $1.5988 \times 10^4 Pa.s$. Finally, the Reynolds number is found to be Reynolds number 3.4750×10^5.

Steps to follow on XFoil.

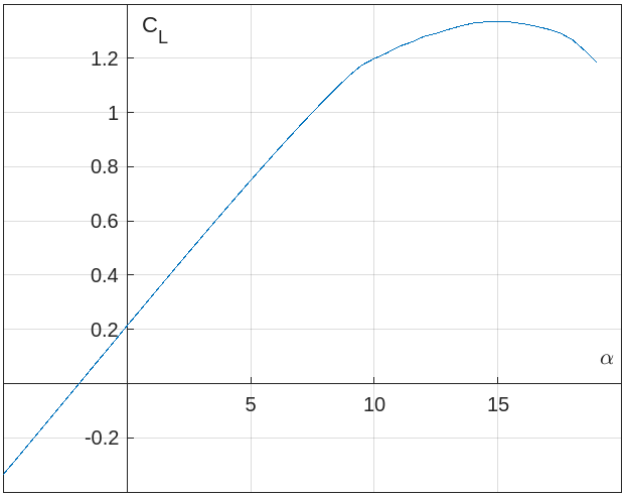

Figure 6: Shows a graph of the lift coefficient against the angle of attack of the NACA 2412 aerofoil.

1. Load in Aerofoil **NACA 2412**
2. Set the Reynolds number to 3.475×10^5
3. Set the boundary layer parameters to transition at 5%
4. Toggle plotting of polar
5. Change iteration count to 100
6. Create polar data for the aerofoil
7. Toggle plotting of the C_p with respect to the length of the aerofoil graph
8. Create the C_p plots for each of the different angles of attack

3.2 Lift coefficient polar

From Figure 6, as the angle of attack increases so does the lift coefficient. Initially, this increase is linear and once boundary layer separation begins due to the increased angle of attack the lift coefficient continues to increase but at a slower rate. At a certain angle of attack, the lift coefficient will be at a maximum and after this point, there is a decrease in the lift coefficient. The zero lift point is at a negative angle of attack, this is the point where the aerofoil produces no lift. any angles lower than this zero lift point cause a more negative lift also known as a downforce on the aerofoil. this is due to the pressure being lower on the lower surface of the wing creating a downwards overall pressure difference and force.

3.3 Drag coefficient polar

The general trend of changing the angle of attack is that as it increases so does the drag, this is shown in Figure 7. From $-5°$ to around $-2°$ there is a slight decrease in the drag. This is because the lift force acting on the aerofoil, although negative is decreasing in magnitude until around $-2°$. Therefore through these angles, the lift-induced drag is also decreasing so the overall drag on the aerofoil is decreasing. From $-2°$ onwards as the angle of attack increases, the drag also increases but this rise is gradual. Until around $9°$ when boundary layer separation begins causing the drag to dramatically increase from this point forth.

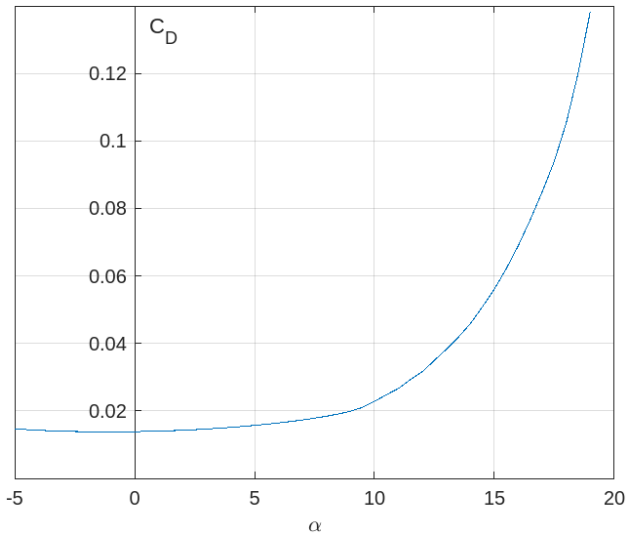

Figure 7: Shows the drag coefficient plotted over a range of angles of attack for the NACA 2412 aerofoil.

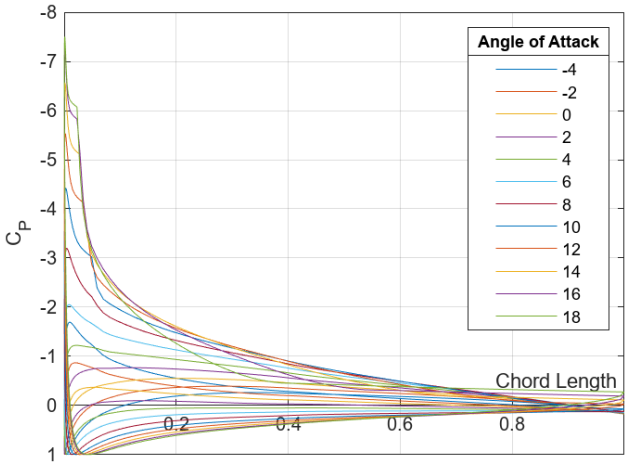

Figure 8: Shows the pressure coefficient across the chordwise length of the aerofoil

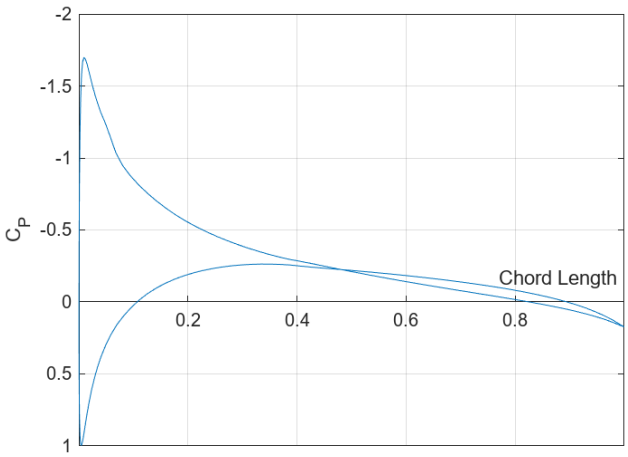

Figure 9: Pressure coefficient over the chord length of the NACA 2412 aerofoil with an angle of attack of $-4°$.

3.4 Chord-wise pressure coefficient graphs

There are some significant angles of attack worth talking about. First let's look at $-4°$, which is shown in more detail in Figure 9. This graph is slightly different to some of the other graphs as the total lift force is negative meaning it is acting downwards. The effect that this has on the C_p plot is that the initial negative spike is on the underside of the wing rather than the upper surface. This means that the suction peak on the aerofoil is on the lower surface so the overall force is negative. One similarity with other angles of attack is at the point that the coefficient of pressure reaches 1 there is a stagnation point on the aerofoil. This happens on the leading edge of the material. By observing Figure 8 there is a noticeable change in the stagnation point as the angle of attack increases. This is shown in greater detail later but as the angle of attack increases the stagnation point moves further along the aerofoil from the leading edge. After the stagnation point, there is a very favourable pressure gradient so the flow will rapidly accelerate until it reaches the most negative pressure or the suction peak. Although the suction peak is on the lower surface of the wing in this case, due to this peak there is still some expansion recovery around the leading edge and the flow will decelerate towards the trailing edge of the wing due to the adverse pressure gradient. At around half chord the lines cross which means that the pressure on the upper surface becomes lower than the pressure on the bottom surface, which will create come positive lift. At the trailing edge of the aerofoil, three is a pressure recovery point where the pressure becomes higher on the aerofoil.

The next interesting angle of attack to observe is at $-2°$; the point where there is zero lift on the wing. The C_p plot for this is shown in Figure 10. By calculating the area between the two curves it is possible to calculate the total force on the aerofoil. From Figure 15 we know that this angle of attack produces $\approx$ zero lift. This graph follows the same pattern as the previous one where the suction peak is on the lower surface of the wing and there is another cross-over point at just over 20% chord. This means that if we calculate the two areas, they will be approximately equivalent thus the force on the wing can be considered zero. After that point, the pressure becomes higher on the upper surface of the wing. This is shown in Figure 11. At this angle, the stagnation point appears to be as far forward as it can be, at the very leading edge of the aerofoil. Past this point, the flow accelerates along both sides of the aerofoil. The acceleration on the lower surface is initially higher as shown by the steeper initial gradient. The pressure does still reach its lowest point on the upper surface with the suction peak at around 20% chord. After the suction peak, the flow follows the same pattern as before just with a more significant effect on the upper surface this time. After the suction peak there is pressure recovery where there is an adverse pressure gradient towards the trailing edge so the flow will decelerate.

At an angle of attack of $4°$, the pressure remains positive across the entire lower surface. This can be seen in Figure 12. From this graph, the transition point also becomes a lot clearer. This has been set at 0.05 or 5% chord and at around this point on the upper surface of the wing there is a slight deviation in the path. This is the point where the flow transitions. By increasing this to this angle of attack the lowest

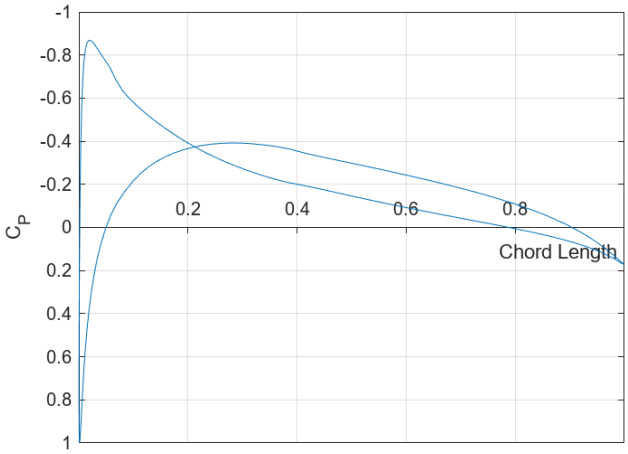

Figure 10: Pressure coefficient over the chord length of the NACA 2412 aerofoil with an angle of attack of $-2°$.

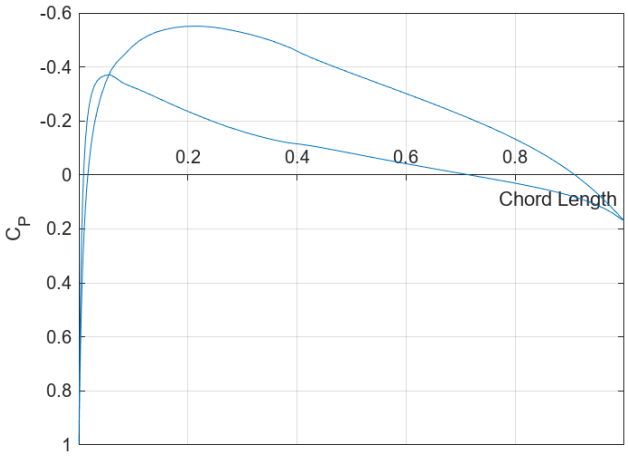

Figure 11: Pressure coefficient over the chord length of the NACA 2412 aerofoil with an angle of attack of $0°$.

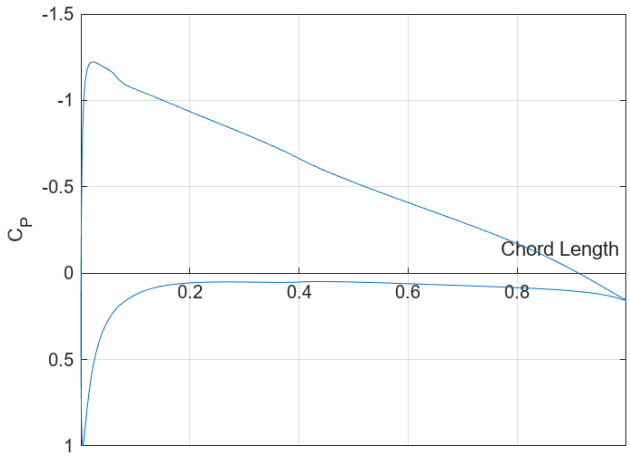

Figure 12: Pressure coefficient over the chord length of the NACA 2412 aerofoil with an angle of attack of 4°.

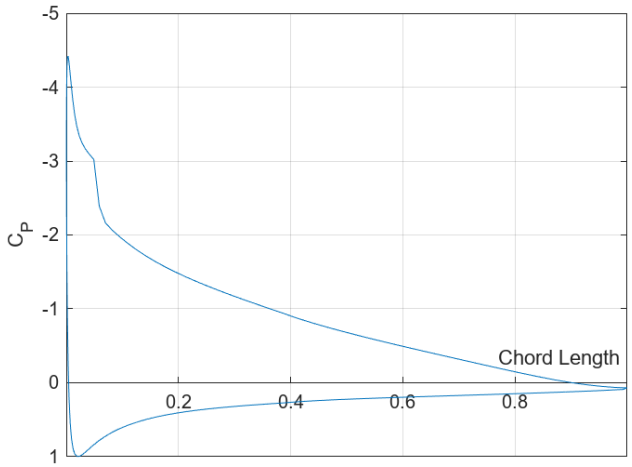

Figure 13: Pressure coefficient over the chord length of the NACA 2412 aerofoil with an angle of attack of 10°.

C_p value increases. This trend can also be seen in Figure 8 as once the angle of attack passes $-2°$ and is continuously increased, the magnitude of the suction peak also increases.

At an angle of attack of 10 degrees flow separation has started to happen. This can be seen from Figure 15. The flow separation point is represented by a flattening off of the pressure coefficient on the upper surface of the wing. From Figure 13 this point is fairly late on along the aerofoil but as the angle of attack increases the separation point moves further towards the front of the aerofoil. This can be seen in Figure 14 where the flat line begins further towards the leading edge of the aerofoil.

From Figure 14 there is also a decrease in the area from an angle of attack of 14° through to 18° this is because the lift is starting to decrease due to the boundary layer separation. As has been mentioned before Figure 14 shows how the stagnation point moves further toward the trailing edge as the angle of attack increases.

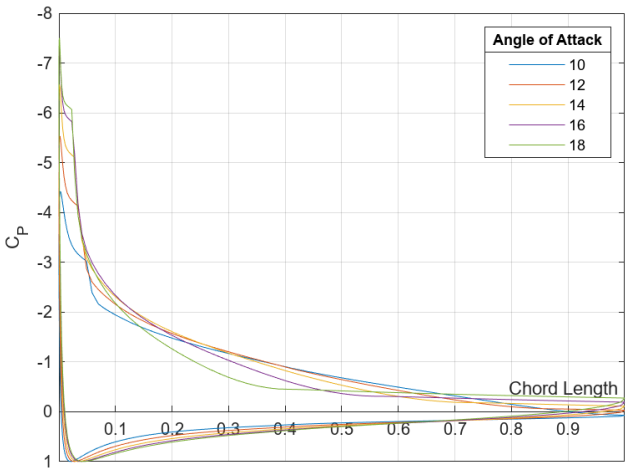

Figure 14: Pressure coefficient over the chord length of the NACA 2412 aerofoil over a range of angle off attack after separation has occurred.

Chord Separation	α°	$R_e \times 10^5$	C_L	C_D	C_M	L/D	N_{cr}
5%	2	3.475	0.4302	0.01428	-0.0460	30.12	9
20%	2	3.475	0.4377	0.01273	-0.0472	34.37	9

Table 3: Data taken from an XFoil simulation to show the effect that changing the position of boundary-layer separation on the aerofoil will have on each of the different aerodynamic properties. The separation position is measured as a percentage of the length of the aerofoil from the leading edge.

4 Question 4 - If boundary-layer transition is moved to 20% chord, what effect does this have on the aerofoil drag coefficient at the cruise condition, and why?

The boundary-layer transition is the point along the aerofoil where the flow across the surface of the aerofoil transitions from laminar to turbulent flow. Changing this boundary-layer position can have large changes to the aerodynamics of an aerofoil. In this case, if we move the transition point to 20% chord from 5% chord then we are moving the transition further downstream away from the leading edge. As a result of this change, the drag will decrease. This means that to continue to cruise at the same speed the aircraft will use less fuel as less force is required from the engines to overcome the lower drag.

We can see the effect of changing the transition point by reviewing the data in 3. It is clear from this data that the drag coefficient decreases, so will the overall drag on the aerofoil. To obtain this data XFoil was used with a constant angle of attack value and only the transition point changed from 5% to 20% chord.

There are several reasons for this decrease in drag. One such reason is that the aerofoil will be subjected to more laminar flow rather than turbulent. Now there will be 20% of the aerofoil with laminar flow rather than 5%. Due to the nature of this type of flow, there will be less interaction between the air and the boundary layer so there will be less skin friction drag acting on the aerofoil. In other words, the viscous effects will be much lower as the boundary layer will be much closer to the surface of the aerofoil. There will also be a much smaller region of turbulent flow so the interaction with the free stream flow will be much less. Which will also lead to the viscous drag decreasing.

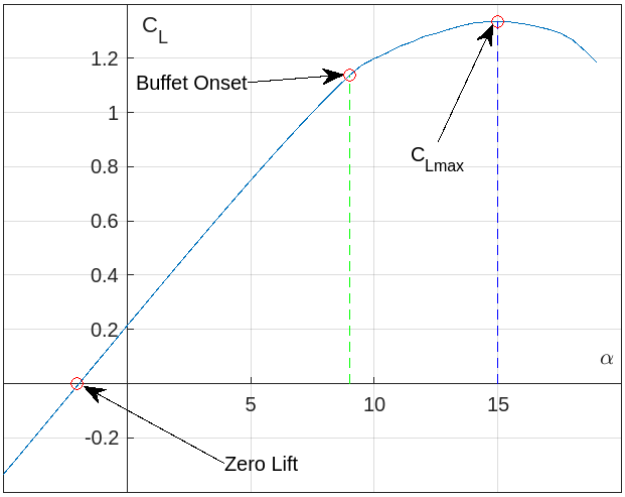

Figure 15: A graph of the lift coefficient, C_L against the angle of attack, α for the NACA 2412 aerofoil generated from the cruise conditions given in 1 being entered into the XFoil software.

5 Question 5 - At the given cruise condition determine the angle of attack corresponding to buffet onset and $C_{L_{max}}$ and provide the supporting evidence (assume 5%c transition). Briefly describe with the aid of diagrams the boundary-layer behaviour at zero-lift, buffet-onset and stall.

The buffet onset is the angle of attack that aerofoil begins to experience flow separation. If we take a look at 6 the $C_{L_{max}}$ is the highest point of the graph which is approximately 1.35 and by reading off from the blue dashed line the angle of attack is approximately 15°. At the point where the graph begins to become non-linear, this is the point where flow separation is beginning to occur. Reading off the red line from 6 this gives a value of the buffet onset to be around 9° Typical values for this aerofoil are from $\alpha \approx 5° - 9°$ which is in line with the value received here [13, slide 26]. From Figure 6 it is also clear that the zero drag coefficient is at around $-2°$ angle of attack. This occurs at the point where the lift coefficient is zero, where the line crosses the x-axis. Thinking about the physics behind the boundary layer at each one of these points we can determine the behaviour of the boundary layer at each of the different conditions. Starting with 0 lift, the boundary layer will not cause any flow separation from the aerofoil. Looking at 17 the flow would remain laminar across the whole aerofoil with the stagnation point at the very tip of the aerofoil. This means that the pressure gradient across the aerofoil is constant so there is no overall force acting on the aerofoil. Considering 16 an attached flow region would be present across the entire aerofoil and there would be no boundary layer separation. The flow will follow a similar pattern to what is happening in this diagram but it will not separate. The pressure gradient between the two sides of the aerofoil will also be zero which means there will be no lift produced from a pressure difference. Next looking at the buffet onset position, for the NACA 2412 aerofoil it occurs at around $\alpha = 9°$ and for the aerofoil in 17 around $\alpha = 5°$ as this is where separation begins to occur. 16 shows the behaviour of the flow across the aerofoil for this angle of attack. First, towards the leading edge of the aerofoil, the flow is laminar and increases in velocity due to the favourable pressure gradient up to the peak of the aerofoil profile. Moving along the chord the boundary layer increases in size and because small disturbances are no longer damped by the laminar flow, they begin to grow and take energy from the laminar flow region. Due to the non-slip condition at the surface of the aerofoil, there will be a friction force between the flow and the surface which will cause disturbances in the flow. These disturbances become small waves and ripples which continue to grow downstream until the flow becomes entirely turbulent. Adding to this once the maximum width of the aerofoil has been exceeded the flow is met with an adverse pressure gradient towards the trailing edge meaning that the flow is caused to

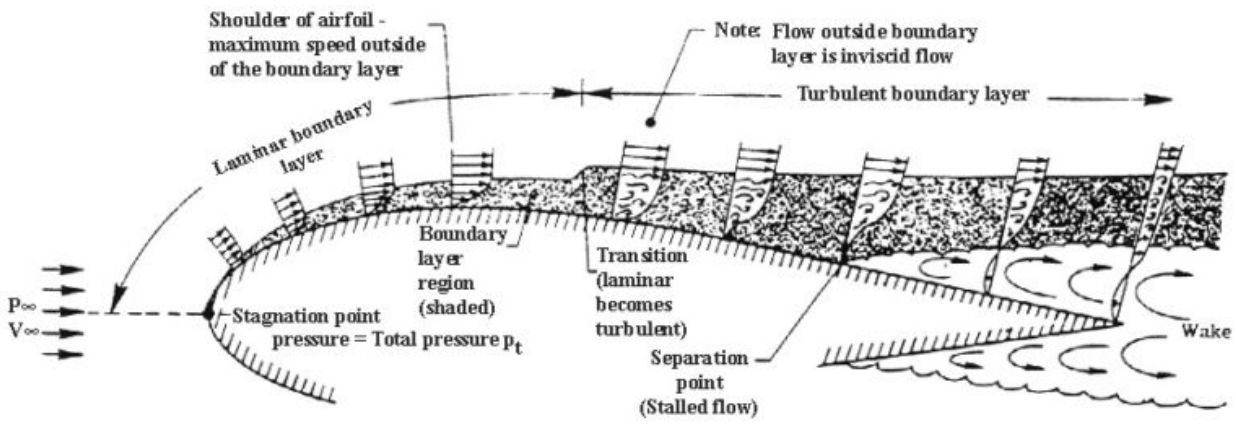

Figure 16: Shows the stages of Boundary layer separation across the top surface of an aerofoil. [2]

slow down. This can be seen in 18 where further downstream the flow reverses. This effect causes boundary layer separation to occur detailed by the 'separation point' label in 16. When this occurs there is a significant loss of lift and increased drag. As the angle of attack is further increased the stall point is reached. This is because the separation point moves further towards the leading edge of the aerofoil resulting in a significant loss of lift. At this point, the stagnation point on the aerofoil will be on the lower surface of the wing. When the flow passes over the tip of the wing there will be a larger angle around the top of the wing. Therefore the geometry will also enable the flow to separate at a point much closer to the leading edge of the aerofoil. There will also be a much larger pressure gradient between these two points so the adverse pressure gradient will be significantly higher and this will cause a lot of pressure drag. The adverse pressure gradient will also cause the separation point to move towards the front of the aerofoil. Due to the increased drag and the loss of the lift at this point, the aerofoil will stall.

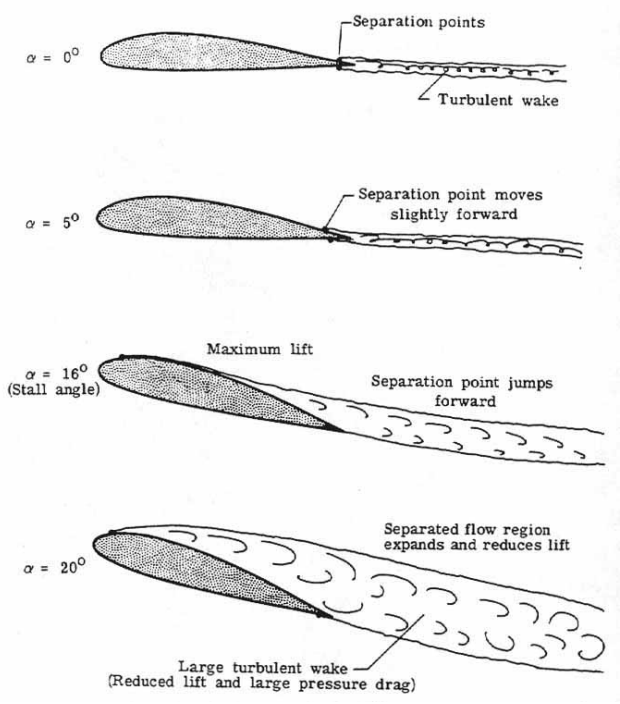

Figure 17: An airfoil whose angle of attack α is being raised from 0° to past the stall angle of attack which in this case is 20°. Below the stall angle, the separation points on the airfoil move towards the leading edge but remain closer to the trailing edge. Near the stall angle, the separation points move rapidly forward causing the pressure drag to rise abruptly. [1]

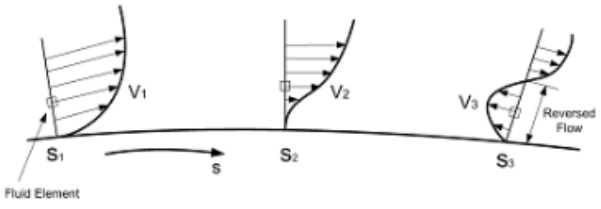

Figure 18: Shows the effect of initially favourable pressure gradients changing to adverse pressure gradients and their effects on the fluid flow. [10]

References

[1] Separation points at different angles of attack, June 2013. [Online; accessed 29. Nov. 2023].

[2] Boundary Layer Separation and Pressure Drag, July 2018. [Online; accessed 29. Nov. 2023].

[3] Air - Dynamic and Kinematic Viscosity, November 2023. [Online; accessed 29. Nov. 2023].

[4] Air Mass/Density, November 2023. [Online; accessed 29. Nov. 2023].

[5] Pressure, November 2023. [Online; accessed 29. Nov. 2023].

[6] John Anderson. *Fundamentals of Aerodynamics*. McGraw-Hill Higher Education, NY, 2016. Available from: ProQuest Ebook Central. [7 December 2023].

[7] M. Drela and M. B. Giles. Viscous-inviscid analysis of transonic and low reynolds number airfoils. *AIAA Journal, 25(10)*, 1987.

[8] Mark Drela. Xfoil: An analysis and design system for low reynolds number aerofoils. Technical report, MIT Dept. of Aeronautics and Astronautics, Cambridge, Massachusetts, 1989.

[9] Mark Drela. *XFOIL 6.9 USER Primer*, 2001.

[10] J. H. Gerrard. Flow around circular cylinders; volume 1. fundamentals. *Journal of Fluid Mechanics*, 350:375–378, 1997.

[11] Cody Lafountain, Kelly Cohen, and Shaaban Abdallah. Use of XFOIL in design of camber-controlled morphing UAVs. *Computer Applications in Engineering Education*, 20(4):673–680, 2012. _eprint: https://onlinelibrary.wiley.com/doi/pdf/10.1002/cae.20437.

[12] Eric Lo. Aerodynamics & aerospace propulsion mech3790 lecture notes. [PDF accessed through Minerva]. MECH3790 Aerodynamics and Aerospace Propulsion. University of Leeds., 2023.

[13] Eric Lo. Boundary layer and integral boundary layer methods. [PowerPoint presentation accessed through Minerva]. MECH3790 Aerodynamics and Aerospace Propulsion. University of Leeds., 2023.

[14] Eric Lo. Mech3790 aerodynamics assignment 2023-24. [PDF accessed through Minerva]. MECH3790 Aerodynamics and Aerospace Propulsion. University of Leeds., 2023.

[15] J. Morgado, R. Vizinho, M.A.R. Silvestre, and J.C. Páscoa. Xfoil vs cfd performance predictions for high lift low reynolds number airfoils. *Aerospace Science and Technology*, 52:207–214, 2016.